Heating and phase transitions of dust-plasma crystals in a flowing plasma

Frank Melandsø*

The Auroral Observatory, University of Tromsø, N-9037 Tromsø, Norway

(Received 6 December 1996)

A three dimensional particle simulation is used to study hexagonal dust crystals in flowing plasmas. The flowing velocity v_0 is mesothermal ($v_{T_i} < v_0 < v_{T_e}$), which is a typical situation for dust particles confined in industrial plasmas and plasma experiments. Unlike for the Yukawa system (Debye-Hückel shielded dust), we find parameter regimes where a hexagonal dust crystal is stable. This is due to the wakefield generated around the individual particles which causes attractive interparticle forces along the axis of the plasma flow. These attractive forces cause a rather strong binding of the crystal since the simulation shows that solid-fluid transitions occur at a much lower Γ value (higher dust temperature) than for the Yukawa system. Stability of a hexagonal dust crystal is found to depend strongly upon the gas neutral pressure since stable crystal structure is obtained for dust-neutral collision frequencies γ_d above some threshold value γ_{d0}. For $\gamma_d < \gamma_{d0}$ the ion flow will excite crystal waves (phonons) where the amplitude of these waves grows as a function of time. This instability will either saturate due to nonlinear lattice waves or continue until the dust crystal structure eventually melts. [S1063-651X(97)02106-5]

PACS number(s): 52.35.Qz, 52.65.−y, 52.40.Hf, 52.25.Kn

I. INTRODUCTION

A Yukawa system, or system of charged particles shielded by a Debye-Hückel potential, has previously been studied by computer simulations in several papers [1–3]. Such a system provides a good model for dust particles embedded in a stationary plasma or in a flowing plasma, as long as the flow velocity v_0 (relative to the dust) is considerably smaller than the ion thermal velocity v_{T_i}. However, as v_0 becomes comparable to or larger than v_{T_i}, an asymmetrical shielding potential occurs around the individual particles, for both subsonic and supersonic flows with respect to the ion-acoustic velocity c_i [4–6]. This implies that a dust particle in industrial plasmas and plasma experiments very seldom can be modeled as a Yukawa system, since dust normally is confined in the regions with $v_0 > v_{T_i}$ (in the sheath or at the sheath edge) [7].

In this paper we introduce a new method for finding the wake or asymmetric potential around dust particles in a mesothermal plasma flow. The method involves computing the eigenvalues to the flow model, which again are used to decouple the linear equations. A linear model for a mesothermal plasma wake contains both an elliptic and a hyperbolic solution [4,5]. The elliptic solution gives a purely repulsive potential between dust particles inserted in this plasma, while the hyperbolic solution has been suggested to cause attractive interparticle forces [8], due to its oscillating nature. It is also believed that the hyperbolic solution, describing ion-acoustic waves excited by the charged dust object, may be the explanation for the observed vertical alignment of dust particles [6,9] in plasma experiments. Here the dust particles, typically, form hexagonal lattices where the particles in in-

dividual hexagonal layers align under each other [10–12].

We examine the stability of such a hexagonal crystal structure by a three dimensional (3D) particle simulation. Plasma simulations like these have previously been applied to 2D crystals [9]. This simulation is, however, the first self-consistent 3D simulation using the interparticle forces generated by the plasma flow. Our simulation shows, for instance, that hexagonal crystal structures may be stable for a sufficiently high neutral pressure. Stability of such a crystal structure will, of course not be found from a Yukawa model, since the stability is strongly correlated to the wakefield around the individual dust particles. To calculate the plasma potential we have to take into account the wakefield from a large number of dust particles, since the individual wakefields will superpose and create an interference pattern. This interference pattern is calculated using periodic boundary conditions.

A very interesting result obtained from the simulations is excitation of crystal waves for a sufficiently low neutral pressure. This observation is in accordance with models presented in Refs. [13] and [14]. The simulations also show that this instability has a profound influence on the dust temperature, and may in some cases melt the dust crystal. It should be noticed that self-excited dust waves also have been observed in experiments [15,16]. Waves like these are likely to be either ionization waves or dust-acoustic-like waves driven by the ion flow [15,16]. Recently Refs. [17] and [18] have pointed out that dust-acoustic flowing instabilities may be present for parameters typical for industrial plasmas and plasma experiments, where both papers were considering weakly coupled dust particles characterized by the Coulomb coupling parameter $\Gamma \ll 1$. Flowing instabilities for weakly coupled dust particles have also been investigated by Ref. [19], using a particle-in-cell simulation. For this paper we show numerically that flowing instabilities are also present in strongly coupled dust plasmas ($\Gamma \gtrsim 1$), and that this instabil-

*Electronic address: frank@phys.uit.no

ity may have a profound influence on both the crystal melting and the final dust temperature.

II. DUST-PLASMA MODEL

The plasma, in our quasiparticle approach, will be described by a two-fluid model including flowing ions and Boltzmann electrons with temperature T_e and density n_e. The 3D ion flow is characterized by density n_i and velocity $\mathbf{v}_i$ which are computed from continuity and force equations. This force equation includes electrostatic force, pressure force from adiabatic ions with temperature T_i, and ion-neutral drag. We will cast the fluid equations into dimensionless forms

$$\partial_T N_i + \nabla_X \cdot (N_i \mathbf{V}_i) = 0, \qquad (1)$$

$$\partial_T \mathbf{V}_i + \mathbf{V}_i \cdot \nabla_X \mathbf{V}_i = \nabla_X \Phi - \epsilon \frac{1}{N_i} \nabla N_i - \gamma \mathbf{V}_i \qquad (2)$$

by introducing normalized variables $T = \omega_{pi} t$, $\mathbf{X} = \mathbf{x}/\lambda_D$, $\mathbf{V}_i = \mathbf{v}_i/c_i$, $N_i = n_i/n_0$, and $\Phi = -e\phi/KT_e$. Time t has here been normalized by the ion plasma frequency $\omega_{pi} = [e^2 Z_i n_0/(\epsilon_0 m_i)]^{1/2}$, where n_0 is the electron density at the plasma potential $\phi = 0$. Distance is normalized by the electron Debye length $\lambda_D = [\epsilon_0 KT_e/(e^2 n_0)]^{1/2}$, and velocity by the cold ion-acoustic velocity $c_i = [Z_i k_B T_e/m_i]^{1/2}$. In Eq. (2) we have also introduced the two normalized variables

$$\epsilon = 3T_i/(Z_i T_e) \quad \text{and} \quad \gamma = \nu_i/\omega_{pi} \qquad (3)$$

giving the ion-electron temperature ratio and dimensionless ion-neutral collision frequency, respectively.

Equations (1) and (2) may now be combined with Poisson's equation, where the space charge contribution from the dust particles is included by N diffuse objects $s_j(\mathbf{x})$ multiplied by their charge number Z_j. Here s_j is normalized with respect to the physical x space. In the X space the Poisson equation yields

$$\nabla_X^2 \Phi = N_i - \exp(-\Phi) + \sum_{j=1}^{N} \frac{Z_j}{n_0 \lambda_D^3} S_j(\mathbf{X}), \qquad (4)$$

where it is convenient to introduce $S_j = \lambda_D^3 s_j$ normalized with respect to the new dimensionless X space $[\int S_j(\mathbf{X}) d\mathbf{X} = 1]$.

To simulate the dust particles we will use a Gaussian distribution

$$S_j = S(\mathbf{X} - \mathbf{X}_j) = \frac{1}{\sigma^3 \pi^{3/2}} \exp[-|\mathbf{X} - \mathbf{X}_j|^2/\sigma^2]. \qquad (5)$$

Such a distribution may, to some extent, simulate finite sized dust particles where the parameter σ corresponds to the dust size in units of λ_D. It is also practical for numerical reasons to use a finite distribution, since the plasma potential obtained from Eq. (4) will be nonsingular in the particle location.

We now separate the linear and nonlinear parts of Eqs. (1)–(4) by introducing the deviations $N_1 = N_i - 1$, $\mathbf{V}_1 = \mathbf{V}_i - \mathbf{V}_0$, and $\Phi_1 = \Phi$ from a homogeneous background flow given by $N_i = 1$, $\mathbf{V}_i = \mathbf{V}_0$, and $\Phi = 0$. The disturbances

created by the dust particles are assumed to be small, so that nonlinear terms may be neglected. For a stationary flow ($\partial_T = 0$) with Mach number M parallel to the Z direction, we obtain, after combining Eqs. (1) and (2),

$$M^2 \partial_Z^2 N_1 = -\nabla_X^2 \Phi_1 + \epsilon \nabla_X^2 N_1 - \gamma M \partial_Z N_1, \qquad (6)$$

$$\nabla_X^2 \Phi_1 = N_1 + \Phi_1 + \sum_{j=1}^{N} \frac{Z_j}{n_0 \lambda_D^3} S(\mathbf{X} - \mathbf{X}_j). \qquad (7)$$

III. ISOLATED DUST PARTICLE

A. Point particle

To solve the fluid equations we will first compute the Green solution where the sum $\sum_{j=1}^{N} Z_j S(\mathbf{X} - \mathbf{X}_j)$ in Eq. (7) is substituted with $-4\pi\delta(\mathbf{X} - \mathbf{X}_j)$. For simplicity we will assume this δ source to be located on the Z axis.

The first step of the solution procedure involves a Fourier transformation $\hat{u}(\mathbf{k}, Z) = (4\pi^2)^{-1} \int u(\mathbf{X}) \exp(-i\mathbf{k} \cdot \mathbf{R}) d\mathbf{R}$ over the direction $\mathbf{R} = (X, Y)$ perpendicular to the flow, with wave number $\mathbf{k} = (k_X, k_Y)$. Equations (6) and (7) then reduce to two coupled ordinary differential equations,

$$M^2 \partial_Z^2 \hat{G}_N = -\hat{G}_N - \hat{G}_\Phi + \pi^{-1}\delta(Z - Z_j) + \epsilon\partial_Z^2 \hat{G}_N - \epsilon k^2 \hat{G}_N$$
$$- \gamma M \partial_Z \hat{G}_N, \qquad (8)$$

$$\partial_Z^2 \hat{G}_\Phi = k^2 \hat{G}_\Phi + \hat{G}_N + \hat{G}_\Phi - \pi^{-1}\delta(Z - Z_j), \qquad (9)$$

where $\hat{G}_N$ and $\hat{G}_\Phi$ are the Fourier transforms of the ion density and plasma potential, respectively.

It is shown in Ref. [4], which neglected ion-neutral collisions ($\gamma = 0$), that Eqs. (8) and (9) contain both an elliptic and a hyperbolic solution. We will show in the Appendix how these two types of solutions may be decoupled for $\gamma = 0$, where the equation set (8) and (9) reduces to

$$\partial_Z^2 \hat{G}_1 = \lambda_+ \hat{G}_1 - \pi^{-1} q_1 \delta(Z - Z_j), \qquad (10)$$

$$\partial_Z^2 \hat{G}_2 = \lambda_- \hat{G}_2 - \pi^{-1} q_2 \delta(Z - Z_j). \qquad (11)$$

Here $[\hat{G}_1, \hat{G}_2]^T$ relates to the Green functions as $\mathcal{P}^{-1}[\hat{G}_N, \hat{G}_\Phi]^T$ where $\mathcal{P}$ is the transformation matrix given in the Appendix [see Eq. (A3)]. The terms λ_+ and λ_- are the eigenvalues for the linear flow equations [Eq. (A2)] while q_1 and q_2 determine the influence of the δ source, as shown in Eqs. (10) and (11). The source coefficients given by Eq. (A6) may be written as

$$q_1 = \frac{1}{\lambda_+ - \lambda_-}\left(\lambda_+ + \frac{\epsilon k^2}{M^2 - \epsilon}\right),$$

$$q_2 = \frac{1}{\lambda_+ - \lambda_-}\left(\lambda_- + \frac{\epsilon k^2}{M^2 - \epsilon}\right). \qquad (12)$$

λ_+, λ_-, q_1, and q_2 will all be functions of the wave number k, the Mach velocity M, and the temperature ratio ϵ given in Eq. (3). Simplified asymptotic solution for $\lambda_\pm$ may also be found for small and large wavelengths. For $k \approx 0$ we get

$$\lambda_\pm \simeq \frac{M^2 - \epsilon - 1 \pm |M^2 - \epsilon - 1|}{2(M^2 - \epsilon)} \qquad (13)$$

while as $k \to \infty$, the eigenvalues approach

$$\lambda_+ \simeq 1 + k^2 \quad \text{and} \quad \lambda_- \simeq -\frac{1 + \epsilon k^2}{M^2 - \epsilon}. \qquad (14)$$

Further on, we will assume $M^2 > \epsilon$, which normally is the case in the regions where dust is confined in gas discharges. This is due to a low T_i/T_e ratio combined with dust confinement in the sheath or in the presheath where the plasma has a significant flowing velocity towards the electrodes. From the Appendix, this yields $\lambda_+ \geq 0$ and $\lambda_- \leq 0$ for all k values where Eqs. (10) and (11) are elliptic and hyperbolic, respectively. Solutions of these equations can easily be obtained, assuming an infinite Z direction, with boundary conditions $\hat{G}_1(-\infty) = 0$, $\hat{G}_1(\infty) = 0$, $\hat{G}_2(-\infty) = 0$, and $\partial_Z \hat{G}_2(-\infty) = 0$ consistent with the elliptic and hyperbolic nature of $\hat{G}_1$ and $\hat{G}_2$, respectively. This yields

$$\hat{G}_1 = \frac{1}{2\pi} \kappa_1^{-1} q_1 \exp(-\kappa_1 |Z - Z_j|), \qquad (15)$$

$$\hat{G}_2 = \begin{cases} \pi^{-1}\kappa_2^{-1} q_2 \sin(\kappa_2 |Z - Z_j|) & \text{if } Z \geq Z_j \\ 0 & \text{if } Z < Z_j, \end{cases} \qquad (16)$$

where $\kappa_1 = \sqrt{\lambda_+}$ and $\kappa_2 = \sqrt{-\lambda_-}$. Finally the Green functions are found from the transformation $[\hat{G}_N, \hat{G}_\Phi]^T = \mathcal{P}[\hat{G}_1, \hat{G}_2]^T$ and by using the inverse Fourier transform. Since the solution is symmetric with respect to the Z axis, it may be written as the integrals

$$G_N = -2\pi \int_0^\infty k(\lambda_- + \lambda_0)\hat{G}_1 J_0(kR)dk$$

$$+ 2\pi \int_0^\infty k(\lambda_+ + \lambda_0)\hat{G}_2 J_0(kR)dk, \qquad (17)$$

$$G_\Phi = 2\pi \int_0^\infty k(\hat{G}_1 - \hat{G}_2)J_0(kR)dk \qquad (18)$$

over the k space where J_0 is the Bessel function of order zero. These integrals must in general be found numerically.

Convergence of integrals (17) and (18) can be investigated by inserting asymptotical λ values [Eq. (14)] in Eqs. (17) and (18) together with $q_1 \simeq 1$ and $q_2 \simeq -1/(M^2 k^2)$ corresponding to large k values. This shows that integral (18) is convergent for all M and ϵ values, except for on the Z axis when $\epsilon = 0$. This is also in agreement with the result in Ref. [4]. The integral (17) is also divergent on the Z axis, even with a finite ion temperature ($\epsilon \neq 0$). We will show in the next section that the divergencies in both of these integrals may be removed by using dust particles with finite size.

B. Gaussian particle

We will now consider solutions from a Gaussian distribution $S(\mathbf{X} - \mathbf{X}_j)$ [Eq. (5)] inserted into Poisson's equation [Eq. (4)]. Unlike for the δ solution, we will also include the case

when the dust object is not centered on the Z axis. This enables us to calculate the total potential field from regular dust crystal structures such as bcc and hexagon, where periodic boundary conditions are applied, and where some of the particles are off the Z axis.

The solution from a single Gaussian given by Eq. (5) may be found by the same procedure as for the δ solution. The N particle source in Eq. (4) is replaced with $-4\pi S(\mathbf{X} - \mathbf{X}_j)$ and Fourier transformed over the direction perpendicular to the flow (X and Y direction). The Fourier transformed equations may then be decoupled into an elliptic ($\hat{G}_1^S$) and a hyperbolic ($\hat{G}_2^S$) part [corresponding to Eqs. (10) and (11)] in the same way as for the δ solution. This gives

$$\partial_Z^2 \hat{G}_1^S = \kappa_1^2 \hat{G}_1^S - \frac{q_1}{\pi^{3/2}\sigma^{1/2}}\exp\left(-\frac{\Delta Z^2}{\sigma^2}\right)f(\mathbf{k}), \qquad (19)$$

$$\partial_Z^2 \hat{G}_2^S = -\kappa_2^2 \hat{G}_2^S - \frac{q_2}{\pi^{3/2}\sigma^{1/2}}\exp\left(-\frac{\Delta Z^2}{\sigma^2}\right)f(\mathbf{k}), \qquad (20)$$

where the index S indicates solution from a Gaussian source. Here we have introduced $\Delta Z = Z - Z_j$ and

$$f(\mathbf{k}) = \exp(-k^2\sigma^2/4)\exp(-ik_X X_j - ik_Y Y_j). \qquad (21)$$

Solution of these two equations may now be found using the same boundary conditions as for the δ solutions $[\hat{G}_1^S(-\infty) = 0, \hat{G}_1^S(\infty) = 0, \hat{G}_2^S(-\infty) = 0, \text{ and } \partial_Z \hat{G}_2^S(-\infty) = 0]$, which gives

$$\hat{G}_1^S = \frac{q_1}{4\pi\kappa_1}\exp\left(\frac{\kappa_1^2\sigma^2}{4}\right)f(\mathbf{k})\left[\exp(-\kappa_1\Delta Z)\mathrm{erfc}\left(\frac{\kappa_1\sigma}{2} - \frac{\Delta Z}{\sigma}\right)\right.$$

$$\left. + \exp(\kappa_1\Delta Z)\mathrm{erfc}\left(\frac{\kappa_1\sigma}{2} + \frac{\Delta Z}{\sigma}\right)\right], \qquad (22)$$

$$\hat{G}_2^S = -\frac{q_2}{2\pi\kappa_2}\exp\left(-\frac{\kappa_2^2\sigma^2}{4}\right)\exp(i\kappa_2\Delta z)f(\mathbf{k})$$

$$\times \mathrm{Im}\left[\mathrm{erfc}\left(-\frac{\Delta Z}{\sigma} - i\frac{\kappa_2\sigma}{2}\right)\right] \qquad (23)$$

written in terms of the complementary error function $\mathrm{erfc}(z) = 2\pi^{-1/2}\int_z^\infty \exp(-t^2)dt$. Here Im denotes the imaginary part of the complex function. Finally these solutions give the density and potential values through the inverse Fourier transform

$$G_N^S = -\int (\lambda_- + \lambda_0)\hat{G}_1^S \exp(i\mathbf{k}\cdot\mathbf{R})d\mathbf{k}$$

$$+ \int (\lambda_+ + \lambda_0)\hat{G}_2^S \exp(i\mathbf{k}\cdot\mathbf{R})d\mathbf{k}, \qquad (24)$$

$$G_\Phi^S = \int (\hat{G}_1^S - \hat{G}_2^S)\exp(i\mathbf{k}\cdot\mathbf{R})d\mathbf{k}. \qquad (25)$$

The function $f(\mathbf{k})$ [Eq. (21)] will now assure that both of these integrals are convergent for $\sigma \neq 0$.

IV. WAKE INTERFERENCE
IN A HEXAGONAL PLASMA CRYSTAL

We will in this section consider the wakefield generated by dust particles in regular dust lattices. Regular dust lattices are frequently observed in dust-plasma experiments due to a large electrostatic energy between the individual particles. Length scales characterizing the spatial periodicity of these crystals are often much smaller than the total extension of the crystal. This allows us to calculate the solution using periodic boundary condition in a computational domain limited by L_X, L_Y, and L_Z, to simulate a medium with infinite extension.

A. Periodic boundary conditions

A plasma potential Φ^p obtained from periodic boundaries may, in principle, be calculated from Eq. (25) by summation over the N Gaussian particles inside the computation domain, and all images of these particles outside the computation box. From a numerical point of view, this method will be enormously time consuming since it requires summation over a large number of particles due to the slow decay of the hyperbolic part of the solution. Instead we suggest expanding the solutions as Fourier series in the X and Y directions, or

$$u(\mathbf{R},Z) = \sum_{l,m} \widetilde{u}(l,m,Z) \exp\left(\frac{2\pi i l X}{L_X} + \frac{2\pi i m Y}{L_Y} \right), \quad (26)$$

which implies periodic boundaries in the X-Y directions.

We will limit ourselves to using distributions with spatial width σ considerably smaller than the size of the computation box. In this case the Fourier coefficients to S will be approximately equal to the one obtained from a Fourier transform. The Fourier coefficients $\widetilde{G}_1$ and $\widetilde{G}_2$ for the elliptic and hyperbolic part of the solution may therefore be found from the previous result, by substituting k_X and k_Y with $2\pi l/L_X$ and $2\pi m/L_Y$, respectively. We also have to solve Eq. (A8) with periodic boundaries in the Z direction instead of the previous boundaries at infinity.

In Fig. 1 we show a wake field produced from periodic boundary condition in all directions. We have here used two particles at $\mathbf{X}_0 = (0,0,0)$ and $\mathbf{X}_1 = (L_X/2, L_Y/2, 0)$ as shown in the uppermost figure. When we use $L_X = \sqrt{3}a$, $L_Y = a$, and $L_Z = d$, these two particles will, together with the periodic boundaries, be equal to an infinite hexagonal crystal. The particle distance within the hexagonal layer will be a while d is the separation distance between the different layers. We show the wakefield or interference pattern, in planes parallel to the X-Y plane, at four different distances L from the upstream layer. At $L=1$ we observe cylindrical symmetric waves in the vicinity of the dust particles (at the center and at the edges) superposed on an interference field.

The interference field becomes dominant at $L=2$ and $L=3$ where a hexagonal interference pattern can be seen, for example, in the shape of the plateau in the center of the figure at $L=2$. It is interesting to notice that this plateau has the same shape as the Brillouin zones for electromagnetic wave diffraction produced by a hexagon.

As an illustration of how the wakefield changes when the interplane distance a is reduced, we have recalculated Fig. 1
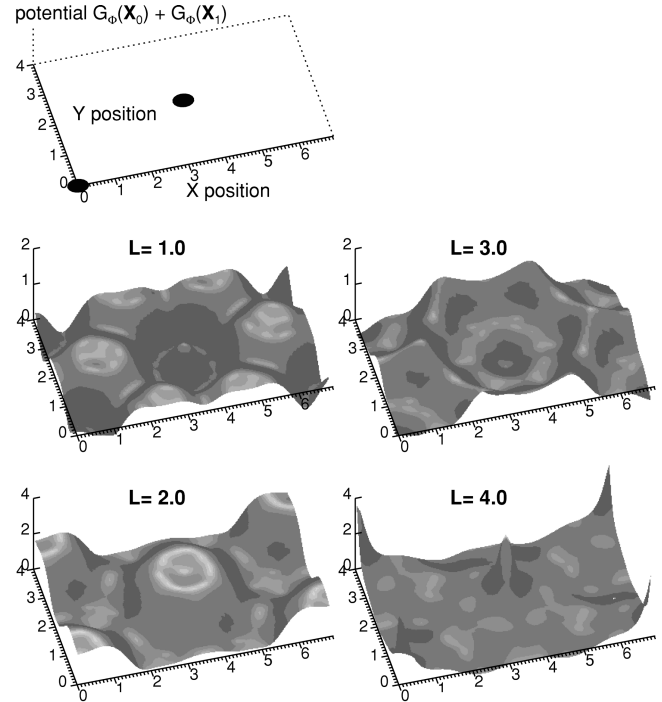

FIG. 1. The plasma potential obtained from ion-acoustic wave interference generated by an infinitely large hexagonal dust crystal. The figures show the wake potential $G^p_\Phi(\mathbf{X}_0) + G^p_\Phi(\mathbf{X}_1)$ in planes perpendicular to the plasma flow at distances L (indicated in the figure) from the upstream layer. One should notice that the figure at $L=4$ is scaled differently than the others. The calculation is done for a subsonic plasma flow with Mach number $M=0.5$ while other parameters are $a=4$, $d=4$, $\epsilon=0.1$, $\sigma=0.2$, and $\gamma=0.075$.

with $a=2$ instead of $a=4$. The result is shown in Fig. 2, where we notice a significant reduction in the interference field generated by the neighbor particles, compared to Fig. 1.

We have also shown in Fig. 3 how the interference field might look, considering a supersonic plasma flow with $M=1.5$. The other parameters in this figure are the same as for Fig. 2. Ion-acoustic wave interference is also seen in Fig. 3, although these are smaller than for the corresponding subsonic flow in Fig. 2. A larger interference field may also be obtained for supersonic flows, by increasing the separation a. This is illustrated in Fig. 4, where we have used the same parameters as in Fig. 3, but increased a to 4. This figure yields a rather complex plasma potential.

B. Plane wave solution

If we consider a subsonic flow and reduce a from the value of 2 used in Fig. 2, to values close to 1, the wakefield becomes less complex, and is close to a plane wave propagating in the direction of the plasma flow (Z direction). These kinds of waves occur only for subsonic flows. For supersonic flows we obtain mainly an exponential damped plasma potential as a approaches 1.

This numerical result can be understood in view of the Fourier transformed equations given in Sec. III A. Plane wave solutions may be found by assuming that the main contribution to the wake comes from wave numbers k close to 0. In this limit we get $q_1 \simeq 0$ and $q_2 \simeq -1$ from Eq. (12) in the case of a subsonic flow. Supersonic flows, on the other
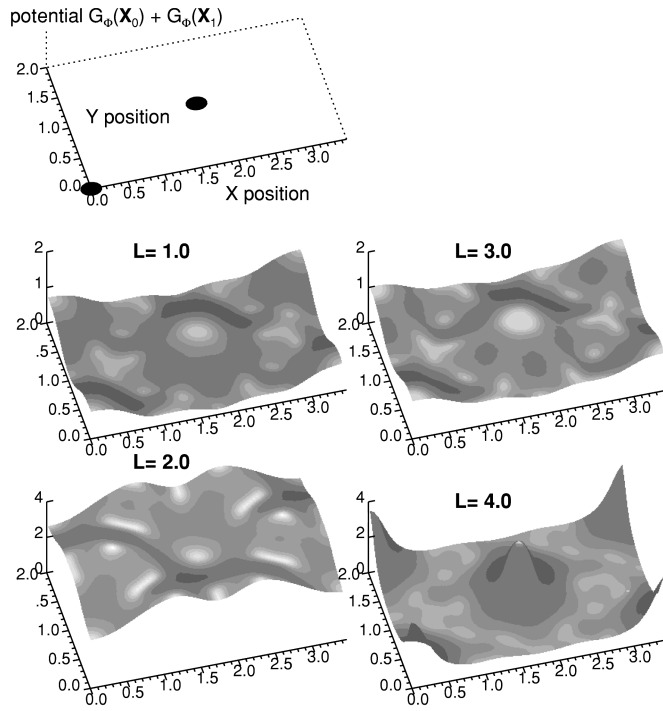
FIG. 2. Plasma potential given by the wake potential $G_\Phi^p(\mathbf{X}_0) + G_\Phi^p(\mathbf{X}_1)$. The calculation is done for the same parameters as in Fig. 1, but with $a = 2$.

hand, yield $q_1 \simeq 1$ and $q_2 \simeq 0$. Since q_1 and q_2 determine the source [see Eq. (12) or (A6)] for the elliptic and hyperbolic part of the solution, respectively, this shows that plane waves may only exist for subsonic flows. The value $k = 0$ also gives, from Eq. (13), a plane wave number
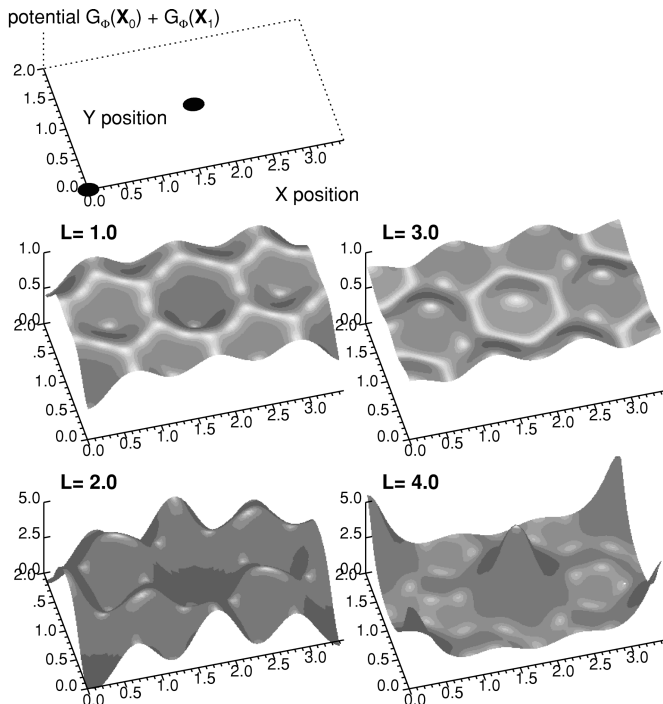

FIG. 3. Plasma potential obtained from a supersonic plasma flow with $M = 1.5$. The other parameters are the same as in Fig. 2.
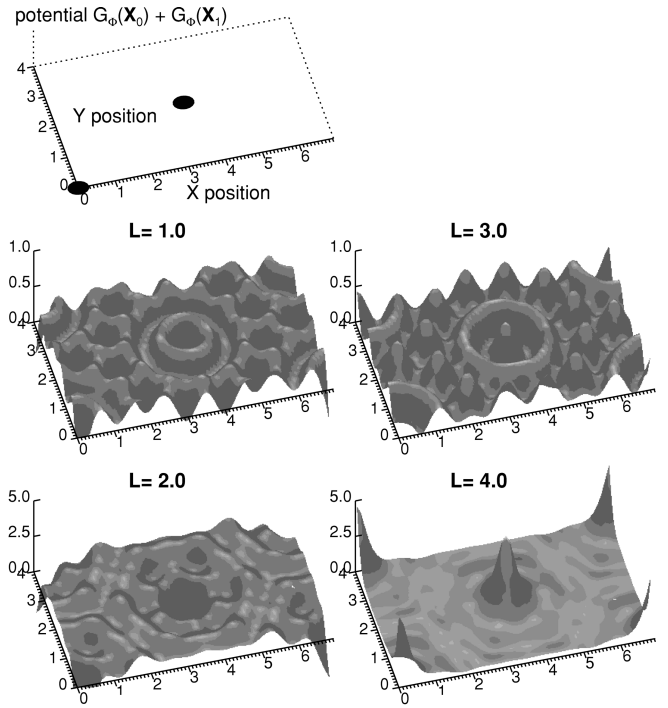

FIG. 4. Calculations done for the same parameters as in Fig. 3, but with $a = 4$.

$$k_0 = \sqrt{-\lambda_-} = \left(\frac{1 - M^2 + \epsilon}{M^2 - \epsilon} \right)^{1/2} \qquad (27)$$

obtained from the negative eigenvalue [see Eq. (13)]. It is also possible to estimate the damping rate of the plane wave due to ion-neutral collisions. This can be done by neglecting the nondiagonal term in Eq. (A8), which yields the damping frequency

$$\gamma_0 = \gamma M \frac{1 - M^2 + \epsilon}{2(M^2 - \epsilon)}. \qquad (28)$$

To find the plane wave solution itself, we will assume small dust particles ($\sigma \ll 1$) where an undamped solution is approximately equal to the δ solution given by Eq. (16). A weakly damped version of this solution generated from a Fourier series instead of a Fourier transform gives the plane wave solution

$$G_\Phi^p = - \frac{8\pi}{\sqrt{3} a^2 k_0} \sum_{n=0}^{\infty} \exp[-\gamma_0(\Delta Z + nd)] \sin[k_0(\Delta Z + nd)] \qquad (29)$$

for a hexagonal crystal. Each term in this sum gives the electrostatic contribution from a hexagonal layer at distance nd. For $\gamma_0 > 0$ this sum will be convergent and gives

$$G_\Phi^p = - \frac{8\pi}{\sqrt{3} a^2 k_0} \frac{1}{D} \{ \exp(-\gamma_0 \Delta Z) \sin(k_0 \Delta Z)$$
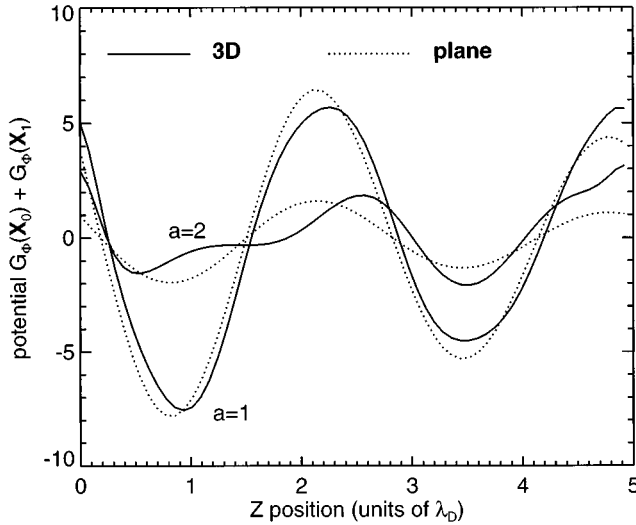$$+ \exp[-\gamma_0(\Delta Z + d)] \sin[k_0(d - \Delta Z)] \}, \qquad (30)$$

where

FIG. 5. The plane wave solution [Eq. (30)] compared to the numerical 3D solution on the Z axis, for $a=1$ and $a=2$. Other parameters which are constant are $M=0.5$, $\epsilon=0.1$, $\gamma=0.075$, $\sigma=0.2$, and $d=5$.

$$D = 1 - 2\exp(-\gamma_0 d)\cos(k_0 d) + \exp(-2\gamma_0 d).$$

From the solution we notice that the amplitude of G_Φ^p will maximize at distances d where $k_0 d = n2\pi$ ($n=1,2,\ldots$). This will be the resonance criterion for the hexagonal crystal which states that the plasma disturbance will maximize when the layer distance d is equal to an integer value n multiplied by the natural wavelength of the plane wave.

In Fig. 5 we compare the values obtained along the Z axis from the numerical 3D solution, with the plane wave solution [Eq. (30)]. For the parameters we refer to the figure caption. The solutions for $a=2$ show some deviation while relatively good agreement is obtained for $a=1$, which indicates an almost plane wakefield for the latter particle spacing.

V. EXCESS ENERGY

An interesting parameter to determine is the excess energy U_{ex} or the energy in excess of the thermal energy of the dust particles. This parameter is interesting since it provides useful information about the thermodynamics of the studied system. For the Yukawa system the excess energy is found to be a function of the parameters

$$\Gamma = Q^2/(4\pi\epsilon_0 \Delta K T_d) \quad \text{and} \quad \kappa = \Delta/\lambda_D \qquad (31)$$

[2,3], where Δ is the average spacing between the dust particles and T_d is the dust temperature. However, for dust crystals in mesothermal flows, the number of independent parameters increases. For the quasiparticle model used in this paper the ion flow field depends on the parameters M, σ, ϵ, and γ [see Eq. (3)]. All of these parameters will now, in addition to Γ and κ, determine U_{ex}.

We will adopt the definition for U_{ex} used in Refs. [2] and [3]. In terms of our Green's function G_Φ^p where p refers to periodic boundaries, this energy may be written as
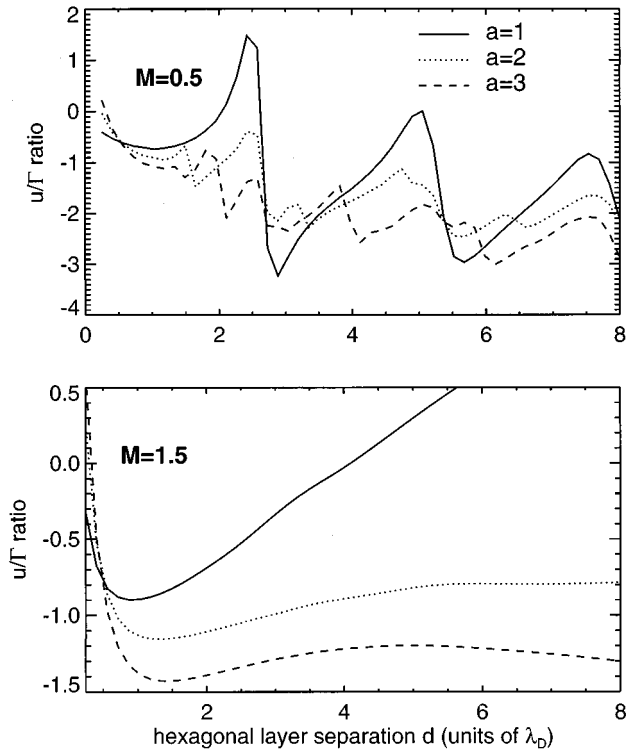

FIG. 6. The ratio between the Madelung energy u and Γ as a function of the distance d between the hexagonal layers. Here the upper figure shows calculations done for $a=1$, $a=2$, and $a=3$, using a subsonic flow velocity ($M=0.5$), while the lower figure shows u/Γ ratios for a supersonic flow ($M=1.5$). In both figures we have used the parameters $\epsilon=0.1$, $\gamma=0.075$, and $\sigma=0.2$.

$$u = \frac{U_{ex}}{NKT_d} = \Gamma\left[\frac{\kappa}{2N}\sum_{i=1}^{N}\sum_{j=1}^{N} G_\Phi^p(\mathbf{X}_i,\mathbf{X}_j) - \frac{3}{2\kappa^2} - \frac{\kappa}{\sqrt{\pi}\sigma}\right]. \tag{32}$$

Here the first term on the right hand side of Eq. (32) gives the average electrostatic energy of the system. From this energy we have to subtract the self-energy which has a finite value for $\sigma\neq 0$ [last term on the right hand side of Eq. (32)]. We also subtract the electrostatic contribution from a uniform charged background [second term on the right hand side of Eq. (32)]. This background term is used in Refs. [2] and [3] to get accordance with previous results for a one component plasma (OCP) in the limit $\kappa\to 0$.

Figure 6 shows the ratio between the excess energy u [Eq. (32)] and the parameter Γ as a function of the separation distance d between the hexagonal layers. The upper and lower figures show u/Γ for a subsonic ($M=0.5$) and supersonic flow ($M=1.5$), respectively, calculated for three different a values ($a=1$, 2, and 3). In the calculations the dust particles are at rest in the equilibrium positions of a hexagonal dust crystal, and the energy is therefore identical to the so-called Madelung energy for the crystal. Thermal motion and crystal phonons will change u (see Refs. [1–3]) so that the values given in Fig. 6, computed from a stationary crystal, only apply to low temperature dust crystals. Other parameters are found in the figure caption.

In the upper part of Fig. 6 we notice several jumps or abrupt changes in u/Γ. These jumps correspond to resonance

distances or distances for constructive interference where waves generated by the individual particles will be in phase. For $a=2$, for example, we observe local minimum values for u/Γ at distances $d\sim 1.2$, 1.7, 2.9, 3.4, ... By using a particle simulation, it is possible to show that hexagonal lattices with d close to some of these minimum values will be stable. As a is reduced to 1 the number of main resonances reduces to 2 (around $d=2.9$ and 5.6). This is mainly because we reduce the complexity of the wave by bringing the particles within the hexagonal layer closer together. At the separation distance $a=1$, the generated wakefield will be nearly a plane wave, as shown in Fig. 5. We also get relatively good agreement between the observed minimum value for u/Γ ($d\sim 2.9$ and 5.6) and theoretical values for the first two resonance distances obtained from Eq. (27) ($d=2\pi/k_0 \simeq 2.63$ and $4\pi/k_0 \simeq 5.26$).

The lower Fig. 6 shows a much less complex behavior of u/Γ where all curves obtain only a single minimum value. Wave resonances as in the upper figure, which produce a large number of minimum values for u/Γ, are not seen, even if d is increased above the maximum value of 8 used in the figure. The reason for this is that the characteristic wavelengths in the supersonic wake are much larger than the one in the subsonic wake. The resonance distances will therefore be located much farther away from the dust particles where the wakefield will be significantly damped for the ion-neutral collision frequency $\gamma=0.075$ used. By reducing γ to, for instance, $\gamma=0.0375$, we are able to observe several minimum values for u/Γ in the same way as for the upper figure.

VI. PARTICLE SIMULATION

Numerical simulations have previously been used to study the Yukawa system where, for instance, the excess energy may be found from simulation together with critical values for the parameters Γ and κ [see Eq. (31)] causing phase transition. Similar methods may now be used to study our flowing plasma system, which has a microscopic shielding potential of the dust particles very different from the Debye-Hückel potential. We will exemplify how the differences between the microscopic potential for these two systems change the stability of hexagonal crystals and the critical Γ value for melting of the crystal.

In the plasma simulation the dust particle j is moved due to the electrostatic force acting on the particle. The force equation may be written in terms of the dimensionless variables $\mathbf{X}$, Φ, and $\tau = \omega_{pd} t$ as

$$\frac{d^2\mathbf{X}_j}{d\tau^2} = \frac{en_0}{Qn}\boldsymbol{\nabla}_X \Phi(\mathbf{X}_j) - \gamma_d \mathbf{V}_j + \mathbf{f}_d. \qquad (33)$$

The time t is normalized with respect to the dust-plasma frequency given in terms of the dust particle charge Q, mass M, and density n, as $\omega_{pd}=[(Q^2 n)/(\epsilon_0 M)]^{1/2}$. The dimensionless velocity $\mathbf{V}_j$ and collision frequency γ_d relate to their physical values $\mathbf{v}_j$ and ν_d, as $\mathbf{v}_j = \lambda_D \omega_{pd} \mathbf{V}_j$ and $\nu_d = \omega_{pd} \gamma_d$, respectively. We have also included a collision term [second term on the right hand side of Eq. (33)] simulating dust-neutral collisions and a force $\mathbf{f}_d$ which is equal, but opposite, to the average electrostatic force acting on the particle [$\mathbf{f}_d = -(en_0/Qn)\Sigma_j \boldsymbol{\nabla}_X \Phi(\mathbf{X}_j)/N$]. This force will

prevent the total crystal structure from being moved by the ion drag, but will, at the same time, not influence the thermodynamical properties of the crystal, since the same force is acting on all particles.

The electrostatic force may be computed from the periodic Green's solution G_Φ^p by adding up the contributions from the N diffuse objects

$$\Phi(\mathbf{X}_j) = -\frac{1}{4\pi\lambda_D^3 n_0}\sum_{i=1}^{N} Z_i G_\Phi^p(\mathbf{X}_j, \mathbf{X}_i). \qquad (34)$$

We will now assume that the number of unit charges Z_i on the dust particle are constant and the same for all dust particles. If we insert this equation in Eq. (33) and express n in terms of the Wigner-Seitz radius Δ ($4\pi\Delta^3 n/3=1$), we obtain

$$\frac{d^2\mathbf{X}_j}{d\tau^2} = -\frac{\kappa^3}{3}\boldsymbol{\nabla}_X \sum_{i=1}^{N} G_\Phi^p(\mathbf{X}_j, \mathbf{X}_i) - \gamma_d \mathbf{V}_j - \mathbf{f}_d, \qquad (35)$$

where $\kappa = \Delta/\lambda_D$. For a hexagonal crystal this parameter may be expressed in terms of dimensionless crystal dimensions a and d as $\kappa=[3\sqrt{3}a^2 d/(8\pi)]^{1/3}$.

Equation (35) is integrated using a Runge-Kutta method of order 4. For each time step we calculated $G_\Phi^p(\mathbf{X}_j, \mathbf{X}_i)$ by using a 3D cubic spline interpolation on the wakefield $G_\Phi^p(\mathbf{0}, \mathbf{X})$ of a particle placed in origin. This wakefield is computed initially in the program and stored in an $N_X \times N_Y \times N_Z$ matrix where N_X, N_Y, and N_Z are the number of uniform discrete values used in the X, Y, and Z directions, respectively.

In the numerical examples we initially place the dust particles in a hexagon with dimensions a and d so that the u/Γ ratio is in the vicinity of one of the local minimum positions shown in Fig. 6. The dust particles are also initially given a random velocity, picked from a Maxwellian distribution. The dust temperature T_d of the distribution is defined as usual, in terms of the statistical variance $3NKT_d/2 = (M/2)\Sigma_j(\mathbf{V}_j - \langle\mathbf{V}\rangle)^2$ where $\langle\cdot\rangle$ denotes the average value. In terms of our dimensionless parameters and from Eq. (31), this relation yields

$$\Gamma = \frac{\kappa^2}{\langle V^2\rangle - \langle\mathbf{V}\rangle\cdot\langle\mathbf{V}\rangle}. \qquad (36)$$

The dust temperature may therefore initially be specified by a Γ value (Γ_0). In the simulation we will also normalize the thermal energy $3NKT_d/2$ in the same way as we did for the excess energy [see Eq. (32)]. This yields

$$u_k = (3NKT_d/2)/(NKT_d) = 3/2. \qquad (37)$$

A. Subsonic plasma flows

We will first use the particle simulation to look at dust crystals in a subsonic plasma flow with Mach number $M=0.5$. A typical result is shown in Fig. 7 where we initially placed $N=128$ particles in a hexagon structure with dimensions $a=2$ and $d=3.41$, and given them Maxwellian
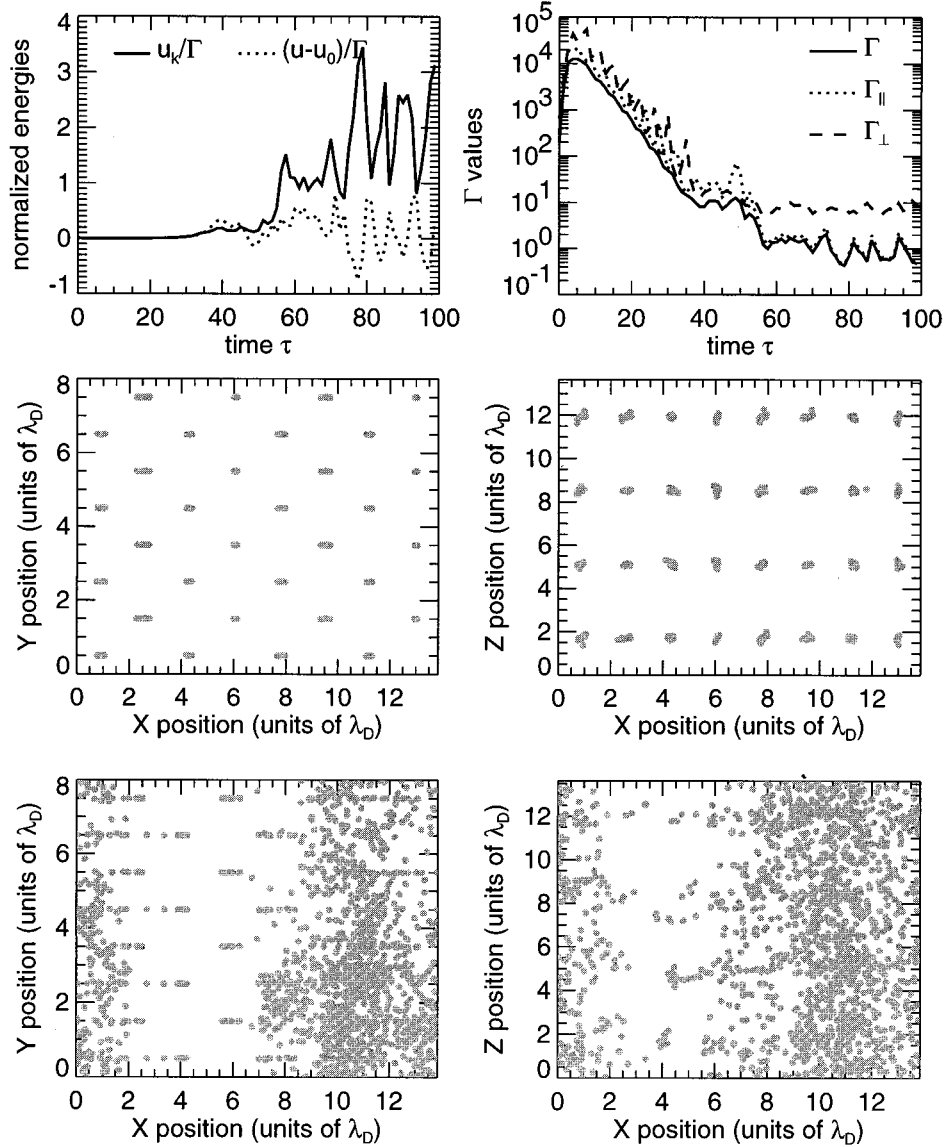
FIG. 7. Particle simulation where $N=128$ dust particles at $\tau=0$ are placed in a hexagonal structure with dimension $a=2$ and $d=3.41$. The dust particles are initially given velocities picked from a Maxwellian velocity distribution with temperature corresponding to $\Gamma=200$. Here the upper left figure shows the time evolution for the ratios u_k/Γ and $(u-u_0)/\Gamma$ where u_k and u are the normalized kinetic energy and excess energy (with value u_0 at $\tau=0$), respectively, while Γ is the Coulomb coupling parameter. The evolution of the latter of these parameters is shown in the upper right figure together with Γ values perpendicular ($\Gamma_\perp$) and parallel ($\Gamma_\parallel$) to the plasma flow. The middle figures show the particle trajectories from $\tau=0$ until $\tau=40$. Here we show in the left the dust trajectories as seen from the top (X-Y plane) where only trajectories from a single dust layer are viewed. A similar side view is shown in middle right figure (X-Z plane). In the lower figures we show the particle trajectories in the remaining part of the simulation (from $\tau=40$ until $\tau=100$) in the same way as for the middle figures. The other parameters used in the simulation are $\epsilon=0.1$, $\gamma=0.075$, $\sigma=0.2$, $M=0.5$, and $\gamma_d=2.3$.

velocities corresponding to $\Gamma=200$. The dust-neutral collision frequency is $\gamma_d=2.3$ while other parameters are found in the figure caption.

The upper left figure shows the evolution of ratios $u_k/\Gamma=3/(2\Gamma)$ and $(u-u_0)/\Gamma$ as a function of time where u is the normalized excess energy [Eq. (32)] with value u_0 at $\tau=0$. The upper right figure shows the parameter Γ as a function of τ [calculated from Eq. (36)] in addition to $\Gamma_\parallel$ and $\Gamma_\perp$ which are calculated as in Eq. (36), but with V replaced with the velocity components parallel and perpendicular to the plasma flow direction. In the middle figures we have shown a top view (left figure) and side view (right figure) of the trajectories generated by particles in a single layer from

time $\tau=0$ until $\tau=40$, while the lower figures show particle trajectories similar to the middle figures from $\tau=40$ until $\tau=100$.

In the initial part of the simulation, from $\tau=0$ to ~ 5, we get a period where the dust temperature decreases (Γ increase in upper right figure). The dust temperature then starts to increase which corresponds to a decrease in the parameter Γ, from 10^4 at $\tau\sim 5$ to 10 at $\tau\sim 40$. We also notice from the upper right figure an almost exponential increase in the temperature in this period, and that the crystals still have not melted at $\tau=40$, as indicated by the middle figures. The reason for the observed increase in the dust temperature is unstable crystal waves (phonons) excited by the flowing
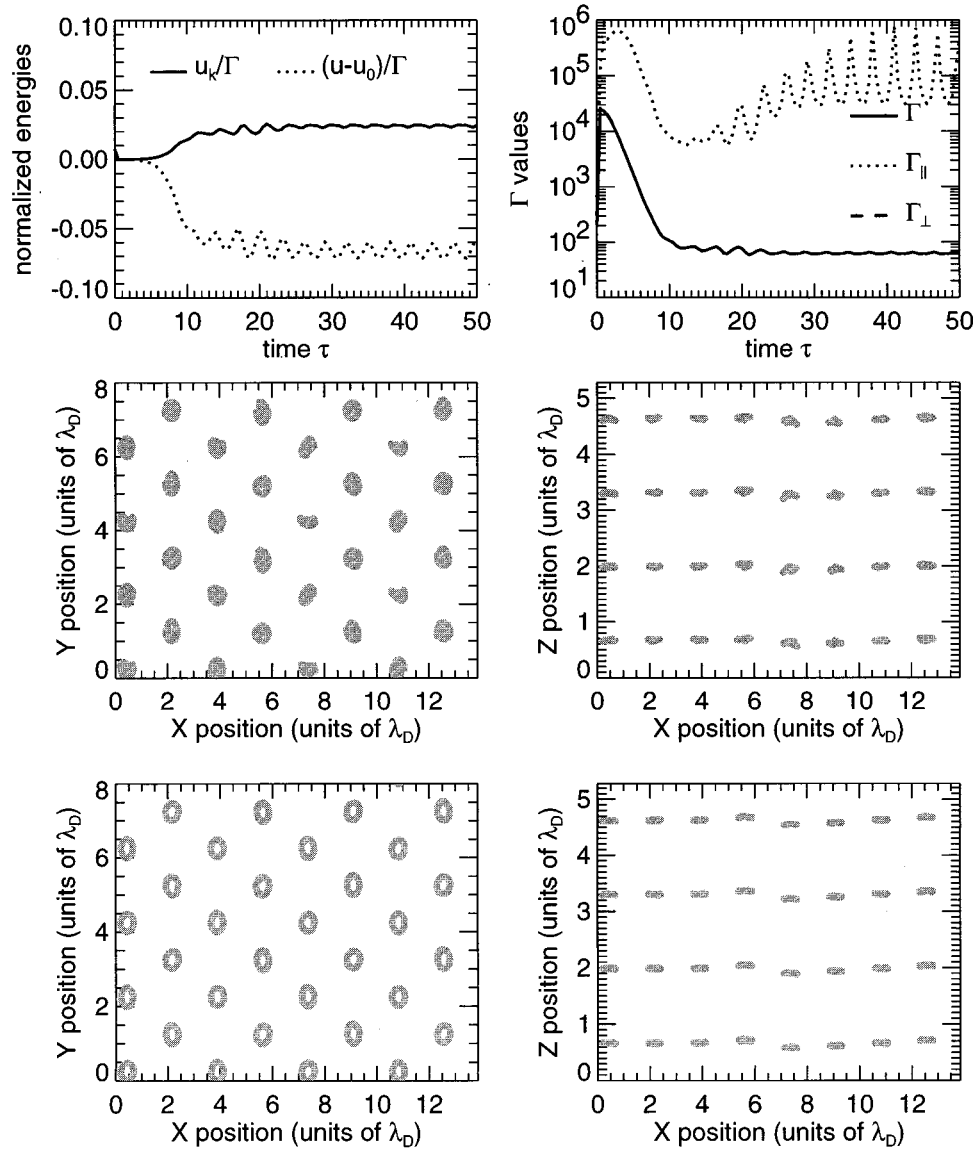
FIG. 8. Particle simulation done in supersonic flow with $M=1.5$. The layer separation is $d=1.32$ while the dust-neutral collision frequency is $\gamma_d=5.0$. All other parameters are the same as in Fig. 7. Here the middle and lower figures show particle trajectories from $0 \leq \tau < 25$ and $25 \leq \tau \leq 50$, respectively.

ions. From $\tau \sim 40$ until ~ 55, the crystal starts to melt with a significant reduction in the crystal wave instability. Around $\tau \sim 55$ there is another jump in the Γ value and the instability finally saturates around $\Gamma \sim 1$. From the lower figures we also see that during the last part of the simulation (from $\tau = 40$ until $\tau = 100$), the crystal becomes completely melted. We also notice that the particles mainly move parallel to the X direction during the melting, which is an indication of crystal waves excited in this particular direction. Wave activity in the X direction is probably also the reason for the nonuniform distribution of particles indicated by the lower figures.

B. Supersonic plasma flows

The dynamic of dust particles may also be simulated in supersonic plasma flows. An example is shown in Fig. 8, where we have used the parameters $M=1.5$, $a=2$, $d=1.32$, and $\gamma_d=5$, while the other parameters are the same

as for Fig. 7. These parameters give a u/Γ ratio in the vicinity of the minimum value shown in the lower Fig. 6. In this simulation we have used a dust-neutral frequency $\gamma_d=5$ which is well below the threshold frequency γ_{d0} for excitation of unstable crystal waves. Unlike the previous simulation, we notice that this instability saturates before the crystal melts. The saturation mechanism here is likely to be of a nonlinear nature. This is because the first part of the instability suggests an exponential growth which gradually diminishes as the dust particle oscillation becomes large, or a typical behavior for systems which are linear unstable but nonlinear stable. This kind of nonlinear stabilization was only seen in the supersonic case.

If we reduce the dust-neutral collision frequency to $\gamma_d=2$ as shown in Fig. 9 we see that nonlinear effects are no longer able to stop the lattice wave instability, and the instability melts the crystal in the same way as in Fig. 7. Similar to the simulation in this figure, we now also get saturation of the instability after melting.
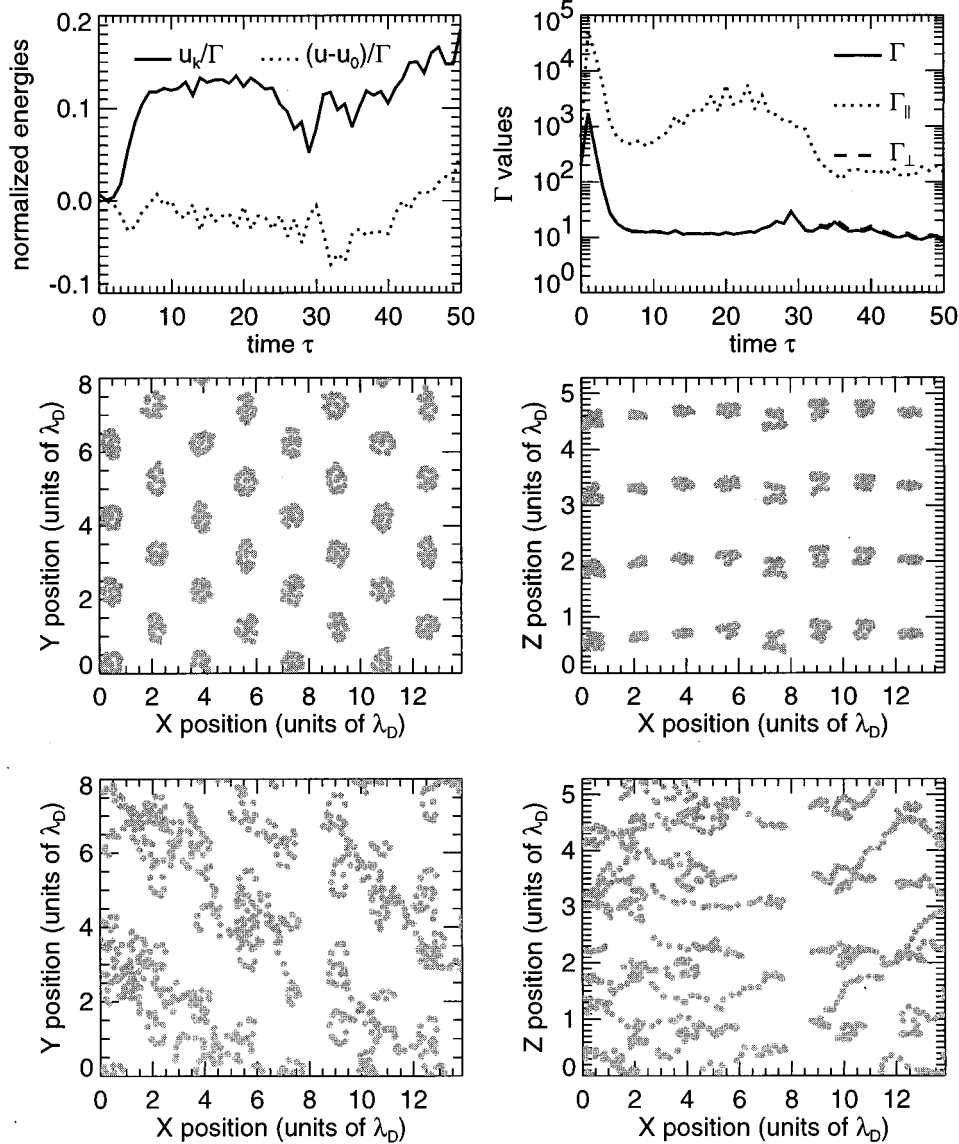
FIG. 9. Particle simulation done for the same parameters as in Fig. 8, but with γ_d reduced to 2.5.

VII. CONCLUSION

We have in this paper shown that our 3D quasiparticle simulation provides good agreement with several experimental results on dust particles confined in gas discharges. Dust-plasma experiments show, for instance, that particles easily crystallize in hexagonal layers aligned on top of each other [10–12]. Stable crystal structures like these are also obtained in the particle simulations as shown in Fig. 8. Stable solution is also found for the parameters used in Fig. 7, if we increase the dust-collision frequency γ_d from the value of 2.3 used to values ≥ 2.6. We have also tested the stability in the vicinity of other local minimum values of u/Γ shown in the upper Fig. 6, and obtained stable solutions for $(a,d)=(1,3)$, $(2,1.7)$, and $(3,6)$, when the dust-neutral collision frequency γ_d is above some threshold value γ_{d0}. This threshold will vary between different crystal dimensions (a,d), and also between simulations where we have kept (a,d) fixed, but changed the number of hexagonal layers, or changed the number of dust particles within a layer.

When the dust-neutral collision frequency γ_d is below the threshold value γ_{d0}, crystal waves with an increasing amplitude appear in the simulations. The initial phase of this instability gives an exponential increase in the dust temperature as, for example, shown from the Γ value in Fig. 7, from $\tau \sim 5$ until $\tau \sim 40$. After this phase, the following two things might happen.

(1) The linear instability enters a nonlinear phase where the instability saturates before the crystal melts. An evolution like this is shown in Fig. 8 and is only observed for supersonic flows.

(2) The instability manages to melt the crystal and saturates after melting, as shown in Figs. 7 and 9. Unlike case (1) where the saturation mechanism is excitation of nonlinear lattice waves, we believe that this saturation is due to the melting itself. As the crystal melts, the phonons will gradually be lost in the crystal and the dust heating becomes less efficient. This also suggests that the streaming instability gives a larger input to the dust kinetic energy in dust crystals than in melted or weakly coupled plasmas as studied in Refs. [17–21].

We believe that the observed crystal instability is driven by the flowing ions due to wave-particle interaction between the plasma fluid and the dust particles, or by the same mechanism as for the previously studied dust-acoustic flowing instability [17–21]. However, all of these papers were only considering weakly coupled dusty plasmas which, of course, does not apply to our strongly coupled dust crystals. A recent paper by Melandsø [22] shows, for instance, that the dispersion relation for dust-acoustic-like waves in a 1D Bravais lattice may be very different from the one obtained in the weakly coupled limit.

The simulation results show that excitation of phonons is crucial for both the melting of the hexagonal crystal and the final dust temperature. How the final dust temperature correlates to the instability can be tested by running simulations with different γ_d values. As γ_d reduces, the crystal instability grows faster with a resulting smaller Γ value (higher dust temperatures) after saturation. It is interesting to notice that excitation of crystal waves also explains the experimentally observed temperature increases in the horizontal plane reported in Ref. [23], in the melting (liquid) and gaseous phases. In these phases the dust temperature is found to be significantly higher than the neutral gas temperature. Heating and melting of the crystal in terms of excited phonons may perhaps also explain why intermediate liquid phases can be stable, since the main energy input (excitation of phonons) is gradually lost as the crystal melts and the particle motion becomes increasingly incoherent.

Oscillation of dust particles, as an important factor for phase transitions, has also previously been studied in Refs. [13] and [14]. Here they consider the stability of two crystal layers with an intermediate ion cloud causing an attractive force acting on dust particles in the downstream layer. It should, however, be noticed that the stability analysis for this system assumes a pure Coulomb potential between the particles, and not the self-consistent potential generated by the plasma flow. The obtained results will therefore only apply to closely packed dust crystals ($\Delta \ll \lambda_D$) since the interparticle potential deviates strongly from a Coulomb field when $\Delta \gtrsim \lambda_D$. This is, for example, clearly seen in Fig. 1, which corresponds to $\Delta \simeq 2.4\lambda_D$.

Another interesting result obtained from Figs. 7 and 9 is the critical Γ value Γ_c for solid-fluid transition. Both figures show Γ_c around ~ 10, or much lower than values for Γ_c obtained in Ref. [3] for bcc crystals with the Yukawa potential. Here they found Γ_c between ~ 172 and 378 for the parameter κ between 0 and 1. However, a recent work by Rosenfeld [24] points out that the Γ_c values given in Ref. [3] are too large, both in view of previous simulations, analytical techniques, and a significant error source detected in Ref. [3]. Reference [24] suggests Γ_c values between ~ 172 and 220 for the κ range used, not far from the result obtained in Ref. [1]. We have also tested our numerical simulation by changing the wakefield potential to a Yukawa potential and found Γ_c much closer to the one given in Refs. [1] and [24] than the transition values given in Ref. [3]. However, it is interesting to observe that the deviations between Refs. [3] and [24] are very small compared to the factor ~ 20–30 difference between the Γ_c found for a wake potential and for a Yukawa potential. This shows that a crystal in a streaming plasma requires a much higher dust temperature before melt-ing than a Yukawa crystal, due to the attractive force in the plasma flowing direction.

An effect which is not incorporated in our model, mainly due to increasing complexity and computation time, is dust charge variation. Dust charge variation is previously found to be important in weakly coupled dust-acoustic waves (DAW), and is therefore likely to be important also in dust crystal waves. This is because the dust charging happened in a time scale much faster than the oscillation period so that the dust charge manages to adjust to the variations in the surrounding plasma. For the DAW, for instance, charge variation is found to give a maximum correction of $\sim 20\%$ in the wave phase velocity, when the dust to electron space charge ratio $|QN/en_e|$ is ~ 1 (see, for instance, Fig. 1 in Ref. [25]). This ratio corresponds to a Havnes P parameter [26] of the order of 1. Previous studies of DAW have also shown that charge variation have a stabilizing effect on streaming instabilities (see, for instance, Ref. [21]). However, this stabilizing effect can probably be neglected in most industrial and experimental plasmas due to the small charging time of dust particles.

APPENDIX DECOUPLING OF THE WAKE EQUATIONS

As previously shown in Refs. [4] and [5], the linear flow equations [Eqs. (6) and (7)] contain both an elliptic and a hyperbolic solution. We will in this appendix show how these two solutions may be decoupled. The decoupled solutions are used to compute the wakefield generated by dust particles in a plane perpendicular to the plasma flow direction Z. Approximate solutions may also be found from the decoupled solutions, for instance, for the plane wave solution considered in Sec. IV.

The Fourier transform of the linear equations [Eqs. (8) and (9)] may be written as the matrix system

$$\partial_Z^2 \mathbf{u} = \mathcal{A}\mathbf{u} - \mathcal{B}\partial_Z\mathbf{u} - \pi^{-3/2}\sigma^{-1}\exp[-(Z-Z_j)^2/\sigma^2]f(\mathbf{k})\mathbf{b}. \tag{A1}$$

Here $\mathbf{u} = [\hat{G}_{Ni}, \hat{G}_\Phi]^T$, $\mathbf{b} = [-(M^2-\epsilon)^{-1}, 1]^T$, $f(\mathbf{k}) = \exp(-k^2\sigma^2/4)\exp(-ik_X X_j - ik_Y Y_j)$,

$$\mathcal{A} = \begin{bmatrix} -(1+\epsilon k^2)(M^2-\epsilon)^{-1} & -(M^2-\epsilon)^{-1} \\ 1 & 1+k^2 \end{bmatrix},$$

and

$$\mathcal{B} = \frac{\gamma M}{M^2-\epsilon}\begin{bmatrix} 1 & 0 \\ 0 & 0 \end{bmatrix}.$$

We will consider cases where the ion-neutral drag does not have a profound influence on the wakefield. In this case the eigenvalues λ to the matrix $\mathcal{A}$ will determine the nature of the solution. From $|\lambda\mathcal{I} - \mathcal{A}| = 0$ we obtain the two eigenvalues

$$\lambda_{\pm} = \frac{1}{2(M^2 - \epsilon)}(\lambda_1 \pm \lambda_2), \tag{A2}$$

where $\lambda_1 = M^2(1 + k^2) - 1 - \epsilon(1 + 2k^2)$ and $\lambda_2 = \{[1 - M^2(1 + k^2) + \epsilon]^2 + 4M^2k^2\}^{1/2}$. The quadratic form inside the curly brackets assures only real λ_2 with $\lambda_2 \geqslant \lambda_1$ for all k and ϵ. In this paper we will consider only plasma flows where $M^2 > \epsilon$ or flowing velocities are larger than the ion-thermal velocity. For this condition, which normally is fulfilled for dust in gas discharges due to a low ion temperature, we have $\lambda_+ \geqslant$ and $\lambda_- \leqslant 0$ for all wave numbers [see Eq. (A2)].

The next step is to diagonalize the matrix $\mathcal{A}$ where the diagonalizing matrix $\mathcal{P}$ and its inverse $\mathcal{P}^{-1}$ are found from the eigenvalues. After some calculations we obtain

$$\mathcal{P} = \begin{bmatrix} -\lambda_- - \lambda_0 & \lambda_+ + \lambda_0 \\ 1 & -1 \end{bmatrix} \tag{A3}$$

and

$$\mathcal{P}^{-1} = \frac{1}{\lambda_+ - \lambda_-} \begin{bmatrix} 1 & \lambda_+ + \lambda_0 \\ 1 & \lambda_- + \lambda_0 \end{bmatrix}, \tag{A4}$$

where $\lambda_0 = (M^2 - \epsilon)^{-1}(1 + \epsilon k^2)$. Equation (A1) may then be transformed to

$$\partial_Z^2 \widetilde{\mathbf{u}} = \mathcal{L}\widetilde{\mathbf{u}} - \widetilde{\mathcal{B}}\partial_Z\widetilde{\mathbf{u}} - \pi^{-3/2}\sigma^{-1}\exp[-(Z - Z_j)^2/\sigma^2]f(\mathbf{k})\widetilde{\mathbf{b}}, \tag{A5}$$

where

$$\widetilde{\mathbf{b}} = \mathcal{P}^{-1}\mathbf{b} = \begin{bmatrix} q_1 \\ q_2 \end{bmatrix} = \frac{1}{\lambda_+ - \lambda_-} \begin{bmatrix} \lambda_+ + \epsilon k^2/(M^2 - \epsilon) \\ \lambda_- + \epsilon k^2/(M^2 - \epsilon) \end{bmatrix}, \tag{A6}$$

$$\widetilde{\mathcal{B}} = \mathcal{P}^{-1}\mathcal{B}\mathcal{P} = \frac{1}{\lambda_+ - \lambda_-} \frac{\gamma M}{M^2 - \epsilon} \begin{bmatrix} -\lambda_- - \lambda_0 & \lambda_+ + \lambda_0 \\ -\lambda_- - \lambda_0 & \lambda_+ + \lambda_0 \end{bmatrix}, \tag{A7}$$

$\widetilde{\mathbf{u}} = [\hat{G}_1, \hat{G}_2]^T = \mathcal{P}^{-1}\mathbf{u}$, while $\mathcal{L}$ is the diagonal matrix diag(λ_+, λ_-). From the diagonalized system [Eq. (A5)] we see that the solution with eigenvalue λ_+ will be elliptic since $\lambda_+ \geqslant 0$, while the eigenvalue $\lambda_- \leqslant 0$ gives a hyperbolic solution. The latter of these solutions is the most interesting one, since it is responsible for spatial oscillations and attractive inter-particle forces.

In the case of an undamped wake ($\gamma = 0$), the two equations in Eq. (A5) will be decoupled. However, when $\gamma \neq 0$, the suggested transformation no longer decouples the equation. For relatively small γ values we suggest using an iteration procedure to calculate $\widetilde{\mathbf{u}}$. This procedure involves dividing the matrix $\widetilde{\mathcal{B}} = \widetilde{\mathcal{B}}_D + \widetilde{\mathcal{B}}_{\mathrm{nd}}$ into matrixes $\widetilde{\mathcal{B}}_D$ and $\widetilde{\mathcal{B}}_{\mathrm{nd}}$ including diagonal and nondiagonal terms, respectively. The solution $\mathbf{u}^{k+1}$ at step $k + 1$ may then be calculated from the solution $\mathbf{u}^k$ at the previous step, as

$$\partial_Z^2 \widetilde{\mathbf{u}}^{k+1} - \mathcal{L}\widetilde{\mathbf{u}}^{k+1} + \widetilde{\mathcal{B}}_D \partial_Z \widetilde{\mathbf{u}}^{k+1}$$

$$= -\pi^{-3/2}\sigma^{-1}\exp[-(Z - Z_j)^2/\sigma^2]f(\mathbf{k})\widetilde{\mathbf{b}} - \widetilde{\mathcal{B}}_{\mathrm{nd}}\partial_Z\widetilde{\mathbf{u}}^k. \tag{A8}$$

Here $k = 0, 1, \ldots, N_{\max}$ with initial solution $\widetilde{\mathbf{u}}^0 = \mathbf{0}$. The left hand side of Eq. (A8) yields decoupled equations, and may therefore be inverted easily.

[1] M. O. Robbins, K. Kremer, and G. S. Grest, J. Chem. Phys. **88**, 3286 (1988).

[2] S. Hamaguchi and R. T. Farouki, J. Chem. Phys. **101**, 9876 (1994).

[3] R. T. Farouki and S. Hamaguchi, J. Chem. Phys. **101**, 9885 (1994).

[4] J. R. Sanmartin and S. H. Lam, Phys. Fluids **14**, 62 (1971).

[5] L. Chen, B. A. Langdon, and M. A. Lieberman, J. Plasma Phys. **9**, 311 (1973).

[6] F. Melandsø and J. Goree, Phys. Rev. E **52**, 5312 (1995).

[7] J. E. Daugherty, R. K. Porteous, and D. B. Graves, J. Appl. Phys. **73**, 1617 (1993).

[8] N. Nambu, S. V. Vladimirov, and P. K. Shukla, Phys. Lett. A **203**, 40 (1995).

[9] F. Melandsø and J. Goree, J. Vac. Sci Technol. A **14**, 511 (1996).

[10] J. H. Chu and I. Lin, Phys. Rev. Lett. **72**, 4009 (1994).

[11] H. Thomas, G. E. Morfill, V. Demmel, J. Goree, B. Feuerbacher, and D. Möhlmann, Phys. Rev. Lett. **73**, 652 (1994).

[12] Y. Hayashi and K. Tachibana, Jpn. J. Appl. Phys. **33**, L804 (1994).

[13] A. Melzer, V. A. Schweigert, I. V. Schweigert, A. Homann, S.

Peters, and A. Piel, Phys. Rev. E **54**, R46 (1996).

[14] V. A. Schweigert, I. V. Schweigert, A. Melzer, A. Homann, and A. Piel, Phys. Rev. E **54**, 4155 (1996).

[15] A. Barkan, R. L. Merlino, and N. D'Angelo, Phys. Plasmas **2**, 3563 (1995).

[16] G. Praburam and J. Goree, Phys. Plasmas **3**, 1212 (1996).

[17] M. Rosenberg, J. Vac. Sci Technol. A **14**, 631 (1996).

[18] N. D'Angelo and R. L. Merlino, Planet. Space Sci. **44**, 1593 (1996).

[19] D. Winske, S. P. Gary, M. E. Jones, M. Rosenberg, V. W. Chow, and D. A. Mendis, Geophys. Res. Lett. **22**, 2069 (1995).

[20] M. Rosenberg, Planet. Space Sci. **41**, 229 (1993).

[21] F. Melandsø, T. K. Aslaksen, and O. Havnes, J. Geophys. Res. **98**, 13 315 (1993).

[22] F. Melandsø, Phys. Plasmas **3**, 3890 (1996).

[23] H. M. Thomas and G. E. Morfill, J. Vac. Sci. Technol. A **14**, 501 (1996).

[24] Y. Rosenfeld, J. Chem. Phys. **103**, 9800 (1995).

[25] F. Melandsø and P. K. Shukla, Planet. Space Sci. **43**, 635 (1995).

[26] O. Havnes, T. K. Aanesen, and F. Melandsø, J. Geophys. Res. **95**, 6581 (1990).